THE JOURNAL OF PHYSICAL CHEMISTRY Letters

Perspective

pubs.acs.org/JPCL

Critical Red Components for Next-Generation White LEDs

Chun Che Lin,[†,‡] Andries Meijerink,[*,‡] and Ru-Shi Liu[*,†,§]

[†]Department of Chemistry, National Taiwan University, Taipei 106, Taiwan

[‡]Condensed Matter and Interfaces, Debye Institute for Nanomaterials Science, Utrecht University, Princetonplein 5, 3584 CC Utrecht, The Netherlands

[§]Department of Mechanical Engineering and Graduate Institute of Manufacturing Technology, National Taipei University of Technology, Taipei 106, Taiwan

ABSTRACT: Warm white LEDs with a high color rendering index and a low correlated color temperature have undergone rapid development. In this regard, red-emitting materials—such as fluoride phosphors, namely, $A_2MF_6:Mn^{4+}$ (A = K, Na, and Cs; M = Si, Ge, Zr, Sn, and Ti) and $XSiF_6:Mn^{4+}$ (X = Ba or Zn), nitridoaluminate phosphor ($Sr[LiAl_3N_4]:Eu^{2+}$), and nanocrystals of cesium lead iodide perovskite ($CsPbI_3$)—have been extensively investigated recently. These compounds generate narrow emissions in the visible red spectral region that are highly perceived by the human eye and lead to excellent chromatic saturation of the red spectra. This paper describes the structure, luminescence properties, morphologies, thermal features, and moisture resistance of critical red components, as well as their limitations for practical applications. This Perspective also provides a basis for future development and scientific challenges in optical research.

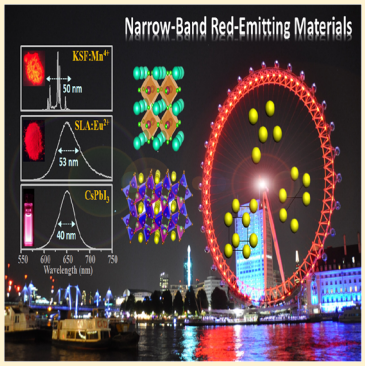

Climate disruption, environmental issues, and considerable energy consumption have gained increased attention worldwide. Lighting requires approximately 19% of the global electricity consumption.[1] Researchers have developed alternative lighting devices to replace traditional illumination lamps to save energy.[2,3] White light-emitting diodes (WLEDs) are the next-generation lighting sources because of their superior properties, such as energy conservation, luminous efficiency, compactness, reliability, long lifetime, and environment friendliness.[4,5] According to a recent report from the US Department of Energy,[6] the potential savings because of a transition to LED technology can reach one-third of the total lighting electricity consumption in the state. High-brightness InGaN blue LEDs are the most substantial innovation in the development of WLEDs and were developed by Isamu Akasaki, Hiroshi Amano, and Shuji Nakamura, who were awarded the 2014 Nobel Prize in Physics for this achievement.

Commercially available phosphor-converted white LEDs (pc-WLEDs) are produced using the $Y_3Al_5O_{12}:Ce^{3+}$ (YAG:Ce) yellow phosphor in combination with blue LEDs through a low cost and simple procedure. YAG:Ce-based WLEDs emit cool white light, which restricts their applications because of low color rendering index (CRI < 80) and high correlated color temperature (CCT = 4000−8000 K). This limitation is caused by the red deficiency of the yellow phosphor and has gained increased research attention. Numerous researchers aim to improve the CRI of pc-WLEDs by using technologies such as novel red-emitting materials for WLEDs.[7−9] Red phosphors, such as those with rare-earth-activated sulfides, molybdate, tungstate, nitrides, and quantum dots (QDs; CdSe, InP, and $CuInS_2$), have yielded warm WLEDs with a high CRI value of 90 and low CTT values ranging from 2700 K to 4000 K.[10−16] The high color saturation and reproducibility of WLEDs render these devices competitive in color perception with inefficient traditional light sources, such as incandescent and halogen bulbs. Nevertheless, the red emitting phosphors also exhibit several limitations, which hinder the performance of these materials for lighting. For example, sulfide phosphors have a limited stability under the operating conditions (temperature and moisture) because of the ionic nature of binary sulfides. Eu^{3+}-activated phosphors possess high CRI values but exhibit low absorption in blue or near-ultraviolet (UV) light because of parity-forbidden 4f−4f transitions. Moreover, nitride phosphors are commercially applied as red components because of their high chemical strength and efficient luminescence; however, their broad emission bands largely limit the maximum achievable luminous efficacies of high-quality warm WLEDs because the spectrum extends into the red spectral region where the eye sensitivity is low. QDs as phosphors are highly promising for WLEDs because of their tunable and narrow emissions, but their commercialization is hindered by their relatively poor chemical and thermal stability.

Available approaches for production of fluorescent materials with high color saturation must be further improved to be suitable for future lighting applications. This paper describes the structure, optical characteristics, morphology, thermal behavior, and chemical stability of narrow-band red-emitting materials, such as fluoride phosphors, namely, $A_2MF_6:Mn^{4+}$ (A = K, Na, and Cs; M = Si, Ge, Zr, Sn, and Ti) and $XSiF_6:Mn^{4+}$

Received: November 1, 2015
Accepted: January 13, 2016
Published: January 13, 2016

DOI: 10.1021/acs.jpclett.5b02433
J. Phys. Chem. Lett. 2016, 7, 495−503

(X = Ba or Zn), nitridoaluminate phosphor ($Sr[LiAl_3N_4]:Eu^{2+}$; SLA), and QDs ($CsPbI_3$). This paper also discusses novel findings, the intrinsic properties of the materials, and an overview of future WLEDs trends.

Crystal structures must be comprehensively analyzed to precisely determine the ideal spectra of the desired luminescent materials.

Structural Symmetry-Induced Narrow-Band Emissions. The use of newly developed red phosphors has been prevalent because of their superior performance in InGaN-based WLEDs. The energy levels of the luminescent centers are influenced by the properties of the host lattice. Figure 1(A) shows the cubic structure of potassium hexafluorosilicate (K_2SiF_6) with a space group of O_h^5–$Fm3m$, where K, Si, and F atoms occupy 2c (Td), 1a (O_h), and 6e (C_{4v}), respectively. Mn^{4+} ions are substituted for Si^{4+} ions in the octahedral site of K_2SiF_6, and the photoluminescence (PL) spectrum [Figure 1D] exhibits characteristic peaks between 600 and 650 nm. The main PL emission peaks are located at 608, 612, 630, 634, and 646 nm, and assigned to electronic/vibronic transitions with energies determined by the local coordination of Mn^{4+} ions. In addition, the optical properties of activators (dopants), such as Eu^{2+} and Ce^{3+} ions, strongly depend on the local structures. The energy of electronic transition decreases for increased covalency between the dopant and the neighboring anions, such as in dopant–N^{3-} bonds and dopant–O^{2-} bonds. The red shift of the emission is known as the nephelauxetic effect. Pust et al.[17] reported the crystal structure of $Sr[LiAl_3N_4]$, which is a part of the triclinic space group $P\bar{1}$ and is isotypic to the $Cs[Na_3PbO_4]$ oxoplumbate.[18] The highly condensed and rigid framework is composed of AlN_4 and LiN_4 tetrahedra, as shown in Figure 1B. The two kinds of crystallographic Sr sites are coordinated by eight N atoms and form a relatively symmetric cuboid-like environment. A narrow emission band is observed for Eu^{2+} ions replacing Sr^{2+} ions. Figure 1(E) illustrates the emission spectrum, with the maximum intensity at 650 nm and a full width at half-maximum (fwhm) of only 53 nm. The PL of nanocrystals (NCs) is readily tunable through compositional modulations and quantum size effects. $CsPbX_3$ perovskites (X = Cl, Br, and I) exhibit several features, such as an exciton Bohr diameter of up to 12 nm, intrinsic bandgap engineering, and cover the entire visible spectral region of 410–700 nm.[19] The corner-sharing octahedra [PbI_6] of $CsPbI_3$ NCs crystallize in the cubic phase, as shown in Figure 1C. The remarkable emission spectrum of $CsPbI_3$ NCs is shown in Figure 1F, where the position and line widths of the main peak are observed at around 650 and 40 nm, respectively. This narrow-band red emission can be ascribed to exciton emission of the host lattice.

Mn^{4+}-Doped Fluoride Materials. Figure 2A illustrates the sharp red emission lines of Mn^{4+}-doped fluoride compounds (K_2TiF_6, Cs_2TiF_6, Na_2TiF_6, and K_2SiF_6). All PL regions are located in the red, between 1.90 and 2.05 eV.[20] The series of peaks can be assigned to electronic-dipole-forbidden transitions ($^2E_g \rightarrow {}^4A_{2g}$) enabled by coupling to vibrational modes, such as ν_3 (stretching), ν_4 (bending), and ν_6 (bending) in the octahedral MnF_6^{2-} of A_2MF_6. These PL spectra are similar, except for the strong zero-phonon line (ZPL) emission of $Na_2TiF_6:Mn^{4+}$ at 2.01 eV. The intensity of ZPL depends on the local symmetry of the surrounding Mn^{4+} ions. As such, Mn^{4+}-activated materials with lower crystal symmetry are expected to show higher ZPL intensities [for example, orthorhombic $KNaSiF_6$ (D^{16}_{2h}–$Pnma$) and trigonal Na_2SiF_6 (D^2_3–$P321$)].[21] The structural properties, schematic energy level diagrams, and

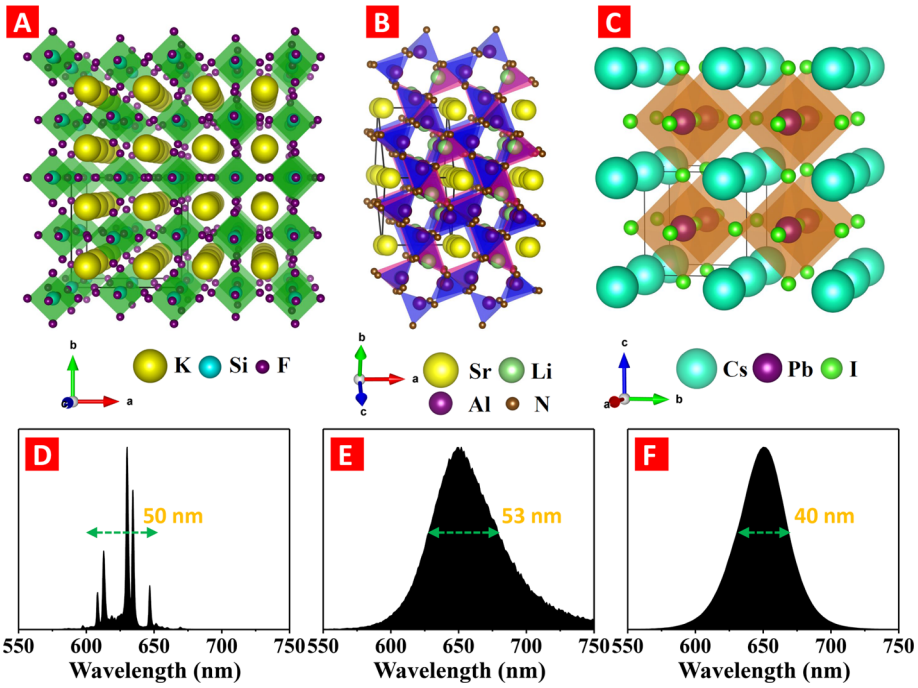

Figure 1. Scheme showing the crystal structures of novel red emitting phosphors (A) K_2SiF_6 fluoride, (B) $Sr[LiAl_3N_4]$ nitridoaluminate, and (C) $CsPbI_3$ perovskite. The black line represents unit cell, and the size of each structure is 2 × 2 × 2. Emission spectra of (D) $K_2SiF_6:Mn^{4+}$, (E) $Sr[LiAl_3N_4]:Eu^{2+}$, and (F) $CsPbI_3$ at room temperature.

DOI: 10.1021/acs.jpclett.5b02433
J. Phys. Chem. Lett. 2016, 7, 495–503

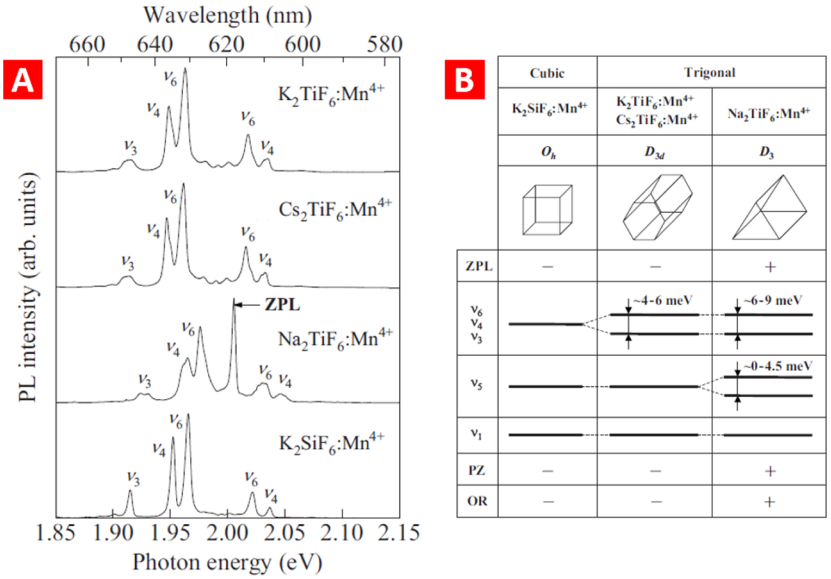

Figure 2. (A) PL spectra of $A_2MF_6:Mn^{4+}$ (A = K, Cs, and Na; M = Ti and Si) at room temperature. (B) Summary of crystal structure, optical property, Raman, piezoelectricity (PZ), and optical rotation (OR) in fluoride compounds. The symbols "+" and "−" indicate strong and weak phenomena, respectively. (Adapted from ref 20.)

Table 1. Key Optical Parameters of Mn^{4+}-Doped Fluoride Materials at Room Temperature

compounds	space group	excitation peaks (nm)	emission peaks (nm)	CIE (*X*, *Y*)	PL lifetime (ms)	ZPL (nm)	reference
K_2SiF_6	cubic O_h^5-*Fm*3*m*	360, 460	597, 608, 613, 630, 634, 646	(0.688, 0.305)	8.1	weak, 621	22−24
Na_2SiF_6	trigonal D_3^2-*P*321	360, 460	594, 604, 609, 626, 630, 642	(0.684, 0.315)	5.1	strong, 617	21, 25, 26
Cs_2SiF_6	cubic O_h^5-*Fm*3*m*	360, 460	612, 616, 633, 637, 650			weak, 624	27
K_2GeF_6	trigonal D_{3d}^3-$P\bar{3}m1$	360, 460	600, 610, 615, 632, 637, 648			strong, 623	28
Na_2GeF_6	trigonal D_3^2-*P*321	360, 460	594, 604, 609, 626, 630, 642	(0.685, 0.315)	3.68	strong, 617	25, 26
Cs_2GeF_6	cubic O_h^5-*Fm*3*m*	360, 460	612, 616, 633, 637, 650			weak, 624	27
K_2ZrF_6	monoclinic C_{2h}^6-*C*2/*c*	354, 459	596, 512, 544			weak, 620	29
Na_2ZrF_6	monoclinic C_{2h}^5-$P2_1/c$						29
Cs_2ZrF_6							
$K_2SnF_6{\cdot}H_2O$	orthorhombic D_{2h}^{24}-*Fddd*	360, 470	599, 608, 613, 629, 634, 646			strong, 621	30
Na_2SnF_6	tetragonal D_{4h}^{14}-$P4_2/mnm$	370, 470	596, 605, 611, 626, 629, 642			weak, 618	31
Cs_2SnF_6	trigonal D_{3d}^3-$P\bar{3}m1$	370, 470	602, 611, 617, 633, 636, 649			weak, 623	31
K_2TiF_6	trigonal D_{3d}^3-$P\bar{3}m1$	364, 459	631, 635, 647		5.8	weak, 620	20, 32
Na_2TiF_6	trigonal D_3^2-*P*321	364, 459	609, 627, 631, 642	(0.685, 0.316)	2.68	strong, 620	20
Cs_2TiF_6	trigonal D_{3d}^3-$P\bar{3}m1$	364, 459	631, 635, 647		3.78	weak, 620	20, 33
$BaSiF_6$	trigonal D_{3d}^5-$R\bar{3}m$	360, 470	615, 632, 648, 650	(0.660, 0.337)	6.5	weak, 624	34, 35
$ZnSiF_6{\cdot}6H_2O$	trigonal C_{3i}^2-$R\bar{3}$	370, 470	612, 616, 633, 637, 650	(0.670, 0.320)	7	weak, 624	36

ZPL, zero-phonon line; CIE, Commission Internationale de l'Éclairage; [blank], no data.

related effects of several fluoride compounds are summarized in Figure 2B. On the basis of the temperature-dependent PL and Raman spectra (T = 20 K),[20] single infrared-active ν_3−ν_6 vibrations in the trigonal environment may split into two infrared-active modes because of small distortions in the octahedral coordination (MnF_6^{2-}). By contrast, ν_1 and ν_2 vibrations only display one infrared-active mode for cubic and trigonal symmetry. Moreover, the electronic-forbidden-transition ZPL of $Na_2TiF_6:Mn^{4+}$ can be activated through piezoelectrically active phonons and q-dependent Fröhlich interaction. These results demonstrate the intimate correlation between the optical characteristics and the structural symmetry class of the host materials. Table 1 presents the comparison of different Mn^{4+}-doped fluoride materials. The two excitation bands of all phosphors are located at ∼360 and ∼460 nm, and the narrow emission lines are centered at ∼620 nm. Hence, these Mn^{4+}-doped fluoride phosphors are potential candidates for UV-based or blue-based WLEDs. However, the feasibility of using $Na_2ZrF_6:Mn^{4+}$ and $Cs_2ZrF_6:Mn^{4+}$ has not yet been reported. Further research must be performed to achieve a breakthrough on zirconium fluoride compounds in the future.

Nitridoaluminate Phosphor Sr[LiAl$_3$N$_4$]:Eu^{2+}. Most commercially available pc-WLEDs contain a blue chip, YAG:Ce yellow phosphor, and $CaAlSiN_3:Eu^{2+}$ red phosphor. This design exhibits advantageous features, such as simple manufacture (no complex electronic circuit needed), full visible spectrum (460−780 nm), and superior thermal properties.[37] Although the $CaAlSiN_3:Eu^{2+}$ red phosphor can be applied in UV and blue LEDs based on the excitation spectrum (light gray curve), the luminous efficacy of this device is low because a considerable fraction of the emission of $CaAlSiN_3:Eu^{2+}$ (dark gray curve) surpasses human eye sensitivity (dashed curve), as shown in

DOI: 10.1021/acs.jpclett.5b02433
J. Phys. Chem. Lett. 2016, 7, 495−503

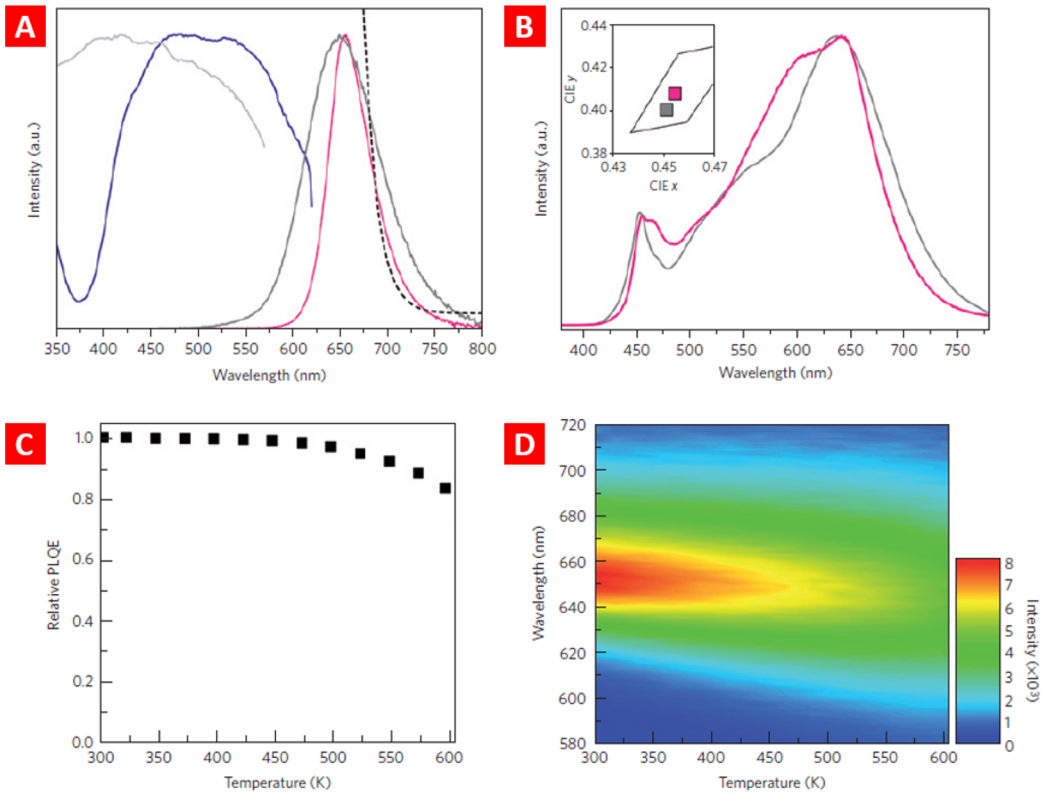

Figure 3. (A) PLE and PL spectra of $Sr[LiAl_3N_4]:4\%Eu^{2+}$ (SLA), (ex, blue curve; em, pink curve) and $CaAlSiN_3:Eu^{2+}$ (ex, light gray curve; em, dark gray curve). The dashed curve represents the sensitivity curve of the human eye. (B) Visible spectra of pc-LEDs with a CCT of 2700 K. Pink curve: blue chip with a mix of green phosphor ($Lu_3Al_5O_{12}:Ce^{3+}$), orange phosphor [$(Ba,Sr)_2Si_5N_8:Eu^{2+}$], and red phosphor (SLA). Gray curve: commercially available high-CRI LEDs. The inset represents the CIE chromaticity coordinates of LEDs. (C) Temperature-dependent PL intensity of SLA. (D) Temperature-dependent emission spectra of SLA. (Adapted from ref 17.)

Figure 3A. By contrast, the emission (pink curve) of $Sr[LiAl_3N_4]:4\%Eu^{2+}$ (SLA) fits well with the curve of human eye sensitivity and exhibits an extremely narrow band (fwhm ~50 nm) for Eu^{2+}-doped materials that emit in the red spectral region. The narrow red emission of SLA can be ascribed to the high symmetrical coordination of the Eu^{2+} activators in the host lattice. However, with respect to the excitation spectrum (blue curve) of SLA, the energy level of $4f^7(^8S_{7/2}) \rightarrow 4f^6(^7F)5d^1$ transitions is only suitable for blue LEDs. In addition, the broad excitation spectrum (400−625 nm) may result in reabsorption of the emissions of other phosphors, such as blue−green $BaSi_2O_2N_2:Eu^{2+}$, green $Lu_3Al_5O_{12}:Ce^{3+}$, and yellow YAG:Ce^{3+}. Figure 3B shows the visible spectrum of a pc-LED (pink curve) with $Lu_3Al_5O_{12}:Ce^{3+}$, $(Ba, Sr)_2Si_5N_8:Eu^{2+}$, and SLA phosphor mixture compared with that of representative high-CRI LEDs (gray curve). The CCT of both pc-LEDs are around 2700 K, as shown in the inset of Figure 3B. The SLA-including pc-LEDs exhibit excellent CRI (R_a8 = 91, $R9$ = 57) and a 14% higher luminous efficacy than the traditional pc-LEDs. The relative integrated PL intensity of the SLA compound as a function of temperature is illustrated in Figure 3C. At 500 K, a 5% decrease in the room-temperature emission of SLA is achieved, which is comparable with those of other nitride compounds with high thermal stability. In Figure 3D, chromaticity changes with increasing environmental temperature are shown. The CIE color coordinates and lumen equivalent (LE) of SLA change from (x, y) = (0.692, 0.306) and LE = 77 lm/W_{opt} (W_{opt} denotes the optical excitation power) to (x, y) = (0.668, 0.330) and LE = 114 lm/W_{opt} as the temperature increases from 303 to 465 K. The emission band of SLA only shifts toward higher energies by ~1 nm and broadens by 374 cm^{-1} from 303 to 465 K. The spectral LE of SLA is easily affected by changing lightly the emission peak position and width in the saturated red spectral range [Figure 3A, dashed curve]. The results indicate that SLA is an outstanding candidate for red-emitting phosphor in pc-LEDs with excellent optical properties, which conform to the sensitivity curve of the human eye.

Cesium Lead Iodide Perovskite $CsPbI_3$ Nanoparticles. Hybrid organic−inorganic perovskites, such as $CH_3NH_3PbI_3$ and $CH_3NH_3PbBr_3$, are prominent compounds used in solar cells, with power conversion efficiencies reaching 20%.[38] These species supply luminescence quantum efficiencies of up to 70% and a tunable band gap. The materials can be synthesized simply through a low-temperature solution procedure.[39] Fully inorganic cesium lead halide perovskites ($CsPbX_3$, X = Cl, Br, and I) are well-known optoelectronic materials that exhibit narrow emission band widths of 12−42 nm, high quantum efficiencies of up to 90%, and radiative lifetimes of 1−29 ns.[19] In the synthesis of red-emitting $CsPbI_3$ cubic NCs, reaction temperature and time are main factors that affect the size and morphology of the product. At 170 °C within the initial 5 s, homogeneous NCs are formed, dominated by cubic particles with sizes ranging from 7 to 15 nm [Figure 4A]. The inset shows that $CsPbI_3$ cubic NCs are single crystalline. The entire visible spectrum (410−700 nm) can be covered by $CsPbX_3$ perovskites, with blue ($CsPbCl_3$), green ($CsPbBr_3$), and red ($CsPbI_3$), and the emission can be adjusted by altering composition and size and thereby the bandgap energy. Figure 4B demonstrates an in situ PL experiment of Br to I exchange in $CsPbBr_3$ through an anion-exchange approach. The red shift

DOI: 10.1021/acs.jpclett.5b02433
J. Phys. Chem. Lett. 2016, 7, 495−503

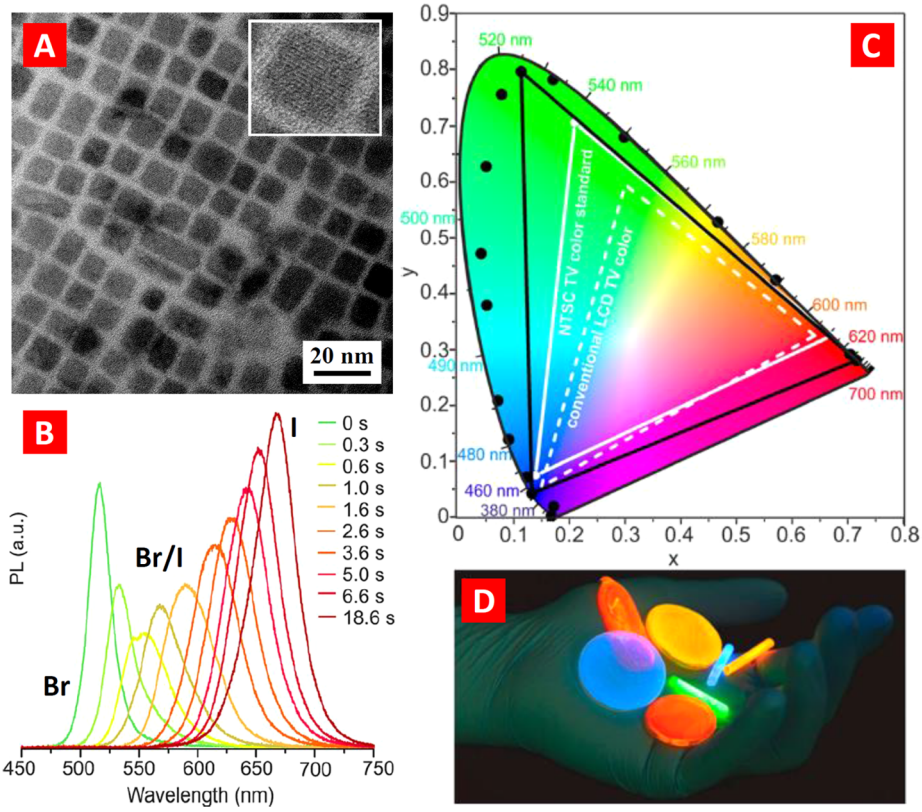

Figure 4. (A) Representative TEM image of $CsPbI_3$ NCs. Scale bar, 20 nm. The inset shows a cubic particle. (B) In situ emissions during $CsPbBr_3$ to $CsPbI_3$ NCs conversion at specific times. (C) CIE 1931 color coordinates of $CsPbX_3$ (X = Cl, Br, and I) NCs. (D) Photograph of $CsPbX_3$ NCs-PMMA polymer monoliths under a UV lamp (λ = 365 nm). (Adapted from refs 19 and 40.)

and broadened width of multiple peaks are ascribed to the continuous phase transition of $CsPbBr_{3-x}I_x$ solid solutions. The PL intensity of narrow red-emitting $CsPbI_3$ is higher than that of the parent sample ($CsPbBr_3$) throughout the procedure. QDs are novel optoelectronic materials for numerous applications, such as displays, backlight, and solid-state lighting.[41] Compared with traditional rare-earth-doped phosphors, QDs exhibit excellent luminescent properties, such as narrow emission band, high quantum efficiency, and color tunability. In Figure 4C, the black dots present the emissions of $CsPbX_3$ NCs plotted on the CIE coordinate diagram. The color gamut of $CsPbX_3$ NCs (solid black triangle) is 40% larger than that of the NTSC TV color standard (solid white triangle), which was identified as 100% by the National Television System Committee in 1951.[42] The high chromaticity can be ascribed to extended green and red areas of the $CsPbX_3$ NCs system. The miscibility of QD emitters and the hybrid organic–inorganic matrix is an important characteristic for practical applications, such as pc-LED devices and solar concentrators. $CsPbX_3$ NCs can be embedded into poly(methylmetacrylate) (PMMA), as shown in Figure 4D. NCs with different colors provide superior optical perspicuity and brilliant emission under UV excitation; hence, perovskites $CsPbX_3$ NCs are promising candidates for next-generation innovative lighting.

LEDs with improved performance can be developed by identifying and improving the limitations of the current devices

Moisture. Circumambient stability issues, especially stability with regard to moisture, temperature and solvents, can be a limitation in the application of luminescent materials. Although red-emitting fluoride phosphors exhibit excellent luminescence properties, their instability under moisture has hindered their applications in the WLEDs industry. Figure 5A shows the fine yellow $K_2SiF_6:Mn^{4+}$ (KSF) powder in ambient atmosphere. However, the degradation of KSF phosphor occurs because Mn ions are desorbed from the host crystal lattice under high-humidity conditions, as depicted in the inset of Figure 5A. At present, a facile approach is used to coat KSF with a moisture-resistant organophosphate layer.[43] KSF is prepared via coprecipitation and subsequent esterification of P_2O_5 with alcohols. This two-step approach can be used to encapsulate the prepared phosphors with transition metal ions as cross-linkers between alkylphosphates. The relative internal quantum efficiency (RIQE = $IQE_t/IQE_{t=0}$ = ~85%) and external quantum efficiency (REQE = $EQE_t/EQE_{t=0}$ = ~87%) of alkylphosphate-coated KSF are significantly higher than those of KSF (RIQE = ~ 57% and *REQE* = ~ 64%) after 30 days of incubation under high temperature and high humidity conditions. A warm WLEDs, which consists of blue chip (λ = 460 nm), YAG:Ce, and alkylphosphate-coated KSF, exhibits a high CRI (R_a = 86, *R*9 = 93) and a luminous efficacy of 79 LmW^{-1}.[43] Figure 5B illustrates pink SLA fine powder in the atmosphere. This SLA powder rapidly decomposes in deionized water (inset). The instability of the SLA phosphor can be explained with the following reaction:

$$SrLiAl_3N_4 + 12H_2O \rightarrow SrLiAl_3(OH)_{12} + 4NH_3 \quad (1)$$

DOI: 10.1021/acs.jpclett.5b02433
J. Phys. Chem. Lett. 2016, 7, 495–503

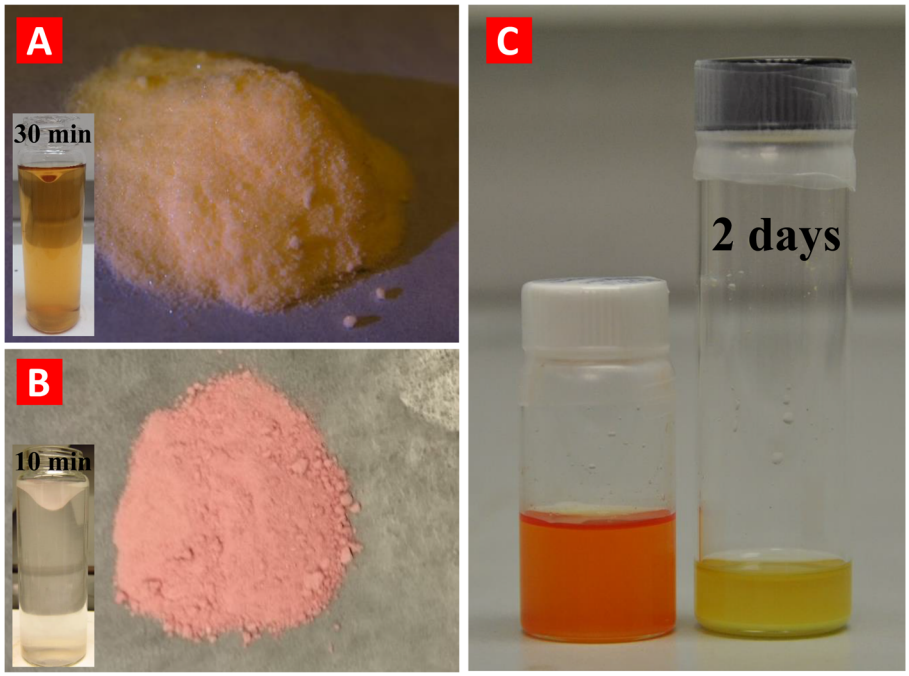

Figure 5. Photographs of (A) K_2SiF_6:Mn^{4+} phosphor, (B) $Sr[LiAl_3N_4]$:Eu^{2+} phosphor, and (C) initial $CsPbI_3$ NCs (left) and $CsPbI_3$ NCs after 2 d (right). The insets of (A) and (B) show the decomposition of powder in deionized water.

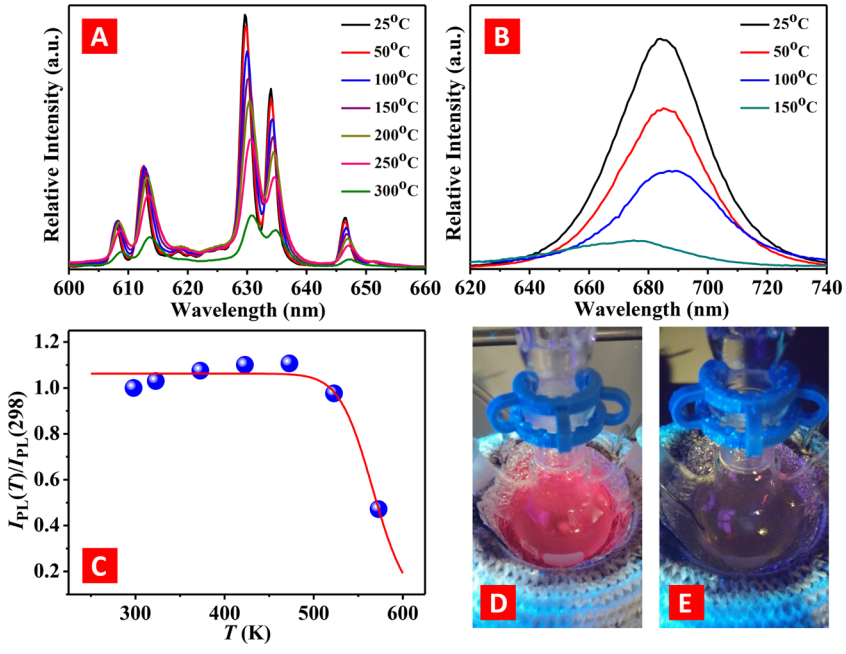

Figure 6. Temperature-dependent PL spectra of (A) K_2SiF_6:Mn^{4+} phosphor and (B) $CsPbI_3$ NCs. (C) Integrated PL ratios $I(T)/I(298)$ of K_2SiF_6:Mn^{4+} measured at temperatures T = 298−573 K. The red line indicates a fit to eq 2. Photographs of $CsPbI_3$ NCs taken under UV irradiation (λ = 365 nm) at the temperatures (D) 25 °C and (E) 150 °C.

We recently improved unstable SLA by coating it with surfactants, such as sodium dodecyl sulfate (SDS), triethylamine, and dodecylamine. The N−H bonds are not easily constituted when a surfactant works as a barrier. In addition, SLA is normally fabricated under high pressure (100 MPa) conditions, such as in hot isotactic pressing solid-state approach. The procedure we used to successfully synthesize SLA under normal pressure (0.92 MPa) can save on production cost.

Stability is also an important issue in application of the new class of perovskite materials, both in solar cells and as phosphors. Monodisperse $CsPbI_3$ NCs (Figure 5C, left side) are produced by solution-phase synthesis, which utilizes the ionic nature of chemical bonding in the system. After incubation of the $CsPbI_3$ NC solution for 2 d, the sample exhibits changes and has no emission, as shown in Figure 5C (right side). This result indicates that $CsPbI_3$ undergoes a phase transition from cubic to orthorhombic during room-temperature processing.[44] For future applications in optoelectronic

DOI: 10.1021/acs.jpclett.5b02433
J. Phys. Chem. Lett. 2016, 7, 495−503

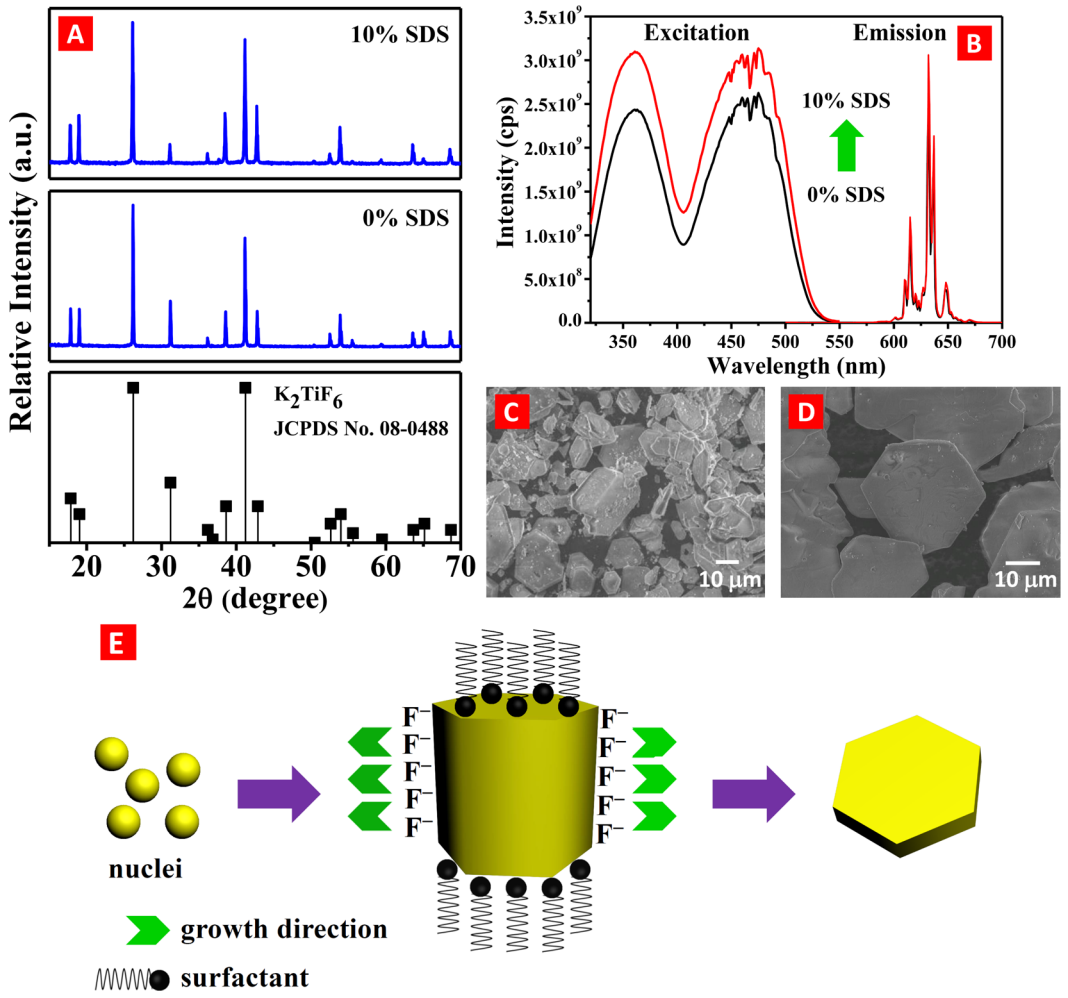

Figure 7. (A) Experimental XRD spectra of 10 wt % SDS-based KTF (top) and pure KTF (middle), and reference XRD patterns (bottom) for trigonal phase of KTF. (B) Typical excitation and emission spectra of 10 wt % SDS-based KTF (red curve) and pure KTF (black curve). Representative SEM images of (C) KTF without SDS and (D) KTF with 10 wt % SDS. (E) Sketch displaying the growth process for KTF prepared with a surfactant.

devices, NCs can be embedded in a polymer, as shown in Figure 4D. The approaches presented in this review can also be employed for unstable materials such as K_2TiF_6:Mn^{4+} phosphor, $Sr[Mg_2Al_2N_4]$:Eu^{2+} phosphor, and $CsPbCl_3$ NCs.

Thermal Stability. Higher temperatures generally reduce a LED's light output because the efficiency of optical materials is restricted by thermal quenching and the degradation rate of LED junction elements is accelerated through higher junction temperatures. Thermal stability of luminescent materials is an important issue in industrial applications in white pc-LEDs systems. Figure 6A shows the temperature dependence of photoluminescence spectra of KSF phosphor. No emission band shift is found and the intensity of emission peaks decreases slightly with increasing temperature. On the contrary, a strong variation in the position and the intensity of emission peaks of $CsPbI_3$ NCs is observed in Figure 6B. At 525 K the integrated emission area of KSF remains 100% compared with that at 298 K, as shown in Figure 6C. The integrated PL ratios $I(T)/I(298)$ can be fitted with the following equation:[31]

$$I_T/I_0 = [1 + D\exp(-E_a/kT)]^{-1} \quad (2)$$

where I_0 is the intensity at $T = 0$ K, k is the Boltzmann constant, and D and the activation energy E_a are refined variables. The activation energy for quenching of KSF is calculated to be approximately 1.4 eV. The thermal quenching of the KSF luminescence is better than for oxynitride phosphors $M_{1.95}Eu_{0.05}Si_{5-x}Al_xN_{8-x}O_x$ (M = Ca, Sr, and Ba).[8] To investigate the quenching behavior of QDs as a function of temperature, $CsPbI_3$ NCs are dispersed in the 1-octadecene. The brilliant red solution is observed clearly when $CsPbI_3$ NCs are kept at room temperature, as shown in Figure 6D. With increasing temperature, the PL intensity of $CsPbI_3$ NCs decreases strongly and it is practically gone above 150 °C, as shown in Figure 6E. The quenched and red-shifted emission band of $CsPbI_3$ NCs can be ascribed to detachment of capping ligands and defect emission, respectively, similar to observations for CdSe QDs.[45] In order to improve thermal stability of QDs, $CsPbI_3$ NCs can be incorporated in polymer matrices such as PMMA [Figure 4D] or poly(lauryl methacrylate), which protects the loss of capping ligands at the surface.

Controlling Morphology and Improving Efficiency. Emitters must be improved to facilitate the development of high-efficiency optoelectronic devices. In this regard, the coating technology offers a potential strategy to fabricate phosphors with superior properties, such as quantum yield, morphology, and chemical stability. Thus, far, brightness enhancement and morphology control of SDS-coated K_2TiF_6:Mn^{4+} (KTF) has

DOI: 10.1021/acs.jpclett.5b02433
J. Phys. Chem. Lett. 2016, 7, 495−503

not yet been reported. In Figure 7A, the X-ray diffraction (XRD) patterns of 10 wt % SDS-based KTF and pure KTF are shown. The diffraction peaks can be assigned to the reference pattern of KTF (trigonal, space group: D_{3d}^3-$P\bar{3}m1$). Even 10 wt % SDS surfactant protects the surface of KTF, and reflections do not significantly shift. As expected for Mn^{4+} ions ($3d^3$ system) in an octahedral crystal field, the excitation and emission spectra [Figure 7B] present two broad bands ($^4A_{2g} \rightarrow {}^4T_{2g}$ and $^4A_{2g} \rightarrow {}^4T_{1g}$ spin-allowed transitions) and narrow bands ($^2E_g \rightarrow {}^4A_{2g}$ spin-forbidden transitions), respectively. The intensity of PLE and PL spectra of KTF can be enhanced by approximately 8% through the application of the SDS surfactant. The scanning electron microscopy (SEM) image of pure KTF in Figure 7C shows rugged particles with varied sizes. By contrast, homogeneous hexagonal sheets are observed in SDS-coated KTF with a particle size of about 40 μm or less, as shown in Figure 7D. On the basis of the SEM images, increased luminescence intensity of the modified KTF can be ascribed to the smooth surface of particles with less defects and refraction. A schematic is plotted in Figure 7E to illustrate the growth mechanism of SDS-coated KTF. Hexagonal sheets are formed through anisotropic growth with SDS surfactant capping.[46,47] The finding confirms that ligands perform an important function in controlling the morphology of as-prepared KTF compounds.

In summary, new narrow-band red-emitting materials for the next generation WLEDs have been reviewed. The materials possess excellent optical properties, which are associated with the nature of the host lattice, such as symmetry, covalency, and rigidity. Further studies must be performed to address the limitations of these phosphors and to develop novel ones through experimental studies and theoretical calculations. Coating technology is a potential avenue for improving properties like stability and efficiency of phosphors to a level that is needed for application in the LED industry. In the future, this method may be applied to other systems to develop new optoelectronic devices.

AUTHOR INFORMATION

Corresponding Authors

*E-mail: a.meijerink@uu.nl. Tel.: +030-2532202. Fax: +030-2532403.

*E-mail: rsliu@ntu.edu.tw. Tel.: +886-2-33661169. Fax: +886-2-23636359.

Notes

The authors declare no competing financial interest.

Biographies

Chun Che Lin is currently working as a postdoctoral associate in Prof. Meijerink's group (Condensed Matter and Interfaces, Debye Institute for Nanomaterials Science, Utrecht University, The Netherlands). He received his B.S. degree in Chemistry from Chung Yuan Christian University in 2005. He received his M.S. and Ph.D. degrees in Chemistry from National Taiwan University in 2007 and 2011, respectively. His current research interests include synthesis of quantum dots and phosphors for light-emitting diodes and bioapplications.

Andries Meijerink is a professor in the Debye Institute for Nanomaterials Science of Utrecht University, The Netherlands. He received his Ph.D. in 1990, and since his appointment at the chair of Solid State Chemistry, he leads an active research in the field of optical spectroscopy of lanthanide ions and quantum dots.

Ru-Shi Liu is a professor at the Department of Chemistry, National Taiwan University. He obtained two Ph.D. degrees in Chemistry, one from National Tsing Hua University in 1990 and the other one from the University of Cambridge in 1992. He worked at the Industrial Technology Research Institute from 1983 to 1985.

ACKNOWLEDGMENTS

The authors are grateful to the Ministry of Science and Technology of Taiwan for financially supporting this research under Contract Nos. MOST 104-2113-M-002-012-MY3, MOST 104-2119-M-002-027-MY3, MOST 104-2923-M-002-007-MY3, and MOST 104-2917-I-564-060.

REFERENCES

(1) Humphreys, C. J. Solid-State Lighting. *MRS Bull.* **2008**, *33*, 459−470.

(2) Lin, C. C.; Zheng, Y. S.; Chen, H. Y.; Ruan, C. H.; Xiao, G. W.; Liu, R. S. Improving Optical Properties of White LED Fabricated by a Blue LED Chip with Yellow/Red Phosphors. *J. Electrochem. Soc.* **2010**, *157*, H900−H903.

(3) Nizamoglu, S.; Zengin, G.; Demir, H. V. Color-Converting Combinations of Nanocrystal Emitters for Warm-White Light Generation with High Color Rendering Index. *Appl. Phys. Lett.* **2008**, *92*, 031102.

(4) Schubert, E. F.; Kim, J. K. Solid-State Light Sources Getting Smart. *Science* **2005**, *308*, 1274−1278.

(5) Chen, L.; Lin, C. C.; Yeh, C. W.; Liu, R. S. Light Converting Inorganic Phosphors for White Light-Emitting Diodes. *Materials* **2010**, *3*, 2172−2195.

(6) Office of Energy Efficiency and Renewable Energy. *Solid-State Lighting Research and Development: Multi-Year Programm Plan*; U.S. Department of Energy: Washington, DC, 2014; http://apps1.eere.energy.gov/buildings/publications/pdfs/ssl/ssl_mypp2014_web.pdf.

(7) Daicho, H.; Iwasaki, T.; Enomoto, K.; Sasaki, Y.; Maeno, Y.; Shinomiya, Y.; Aoyagi, S.; Nishibori, E.; Sakata, M.; Sawa, H.; et al. A Novel Phosphor for Glareless White Light-Emitting Diodes. *Nat. Commun.* **2012**, *3*, 1132−1139.

(8) Chen, W. T.; Sheu, H. S.; Liu, R. S.; Attfield, J. P. Cation-Size-Mismatch Tuning of Photoluminescence in Oxynitride Phosphors. *J. Am. Chem. Soc.* **2012**, *134*, 8022−8025.

(9) Im, W. B.; George, N.; Kurzman, J.; Brinkley, S.; Mikhailovsky, A.; Hu, J.; Chmelka, B. F.; DenBaars, S. P.; Seshadri, R. Efficient and Color-Tunable Oxyfluoride Solid Solution Phosphors for Solid-State White Lighting. *Adv. Mater.* **2011**, *23*, 2300−2305.

(10) Ronda, C. *Luminescence-from Theory to Applications*; Wiley-VCH: Weinheim, Germany, 2007; pp 77−289.

(11) Neeraj, S.; Kijima, N.; Cheetham, A. K. Novel Red Phosphors for Solid-State Lighting: The System $NaM(WO_4)_{2-x}(MoO_4)_x:Eu^{3+}$ (M = Gd, Y, Bi). *Chem. Phys. Lett.* **2004**, *387*, 2−6.

(12) Long, S.; Hou, J.; Zhang, G.; Huang, F.; Zeng, Y. High Quantum Efficiency Red-Emission Tungstate Based Phosphor $Sr-(La_{1-x}Eu_x)_2Mg_2W_2O_{12}$ for WLEDs Application. *Ceram. Int.* **2013**, *39*, 6013−6017.

(13) Li, Y. Q.; Van Steen, J. E. J.; Van Krevel, J. W. H.; Botty, G.; Delsing, A.; Disalvo, F.; Dewith, G.; Hintzen, H. Luminescence Properties of Red-Emitting $M_2Si_5N_8:Eu^{2+}$ (M = Ca, Sr, Ba) LED Conversion Phosphors. *J. Alloys Compd.* **2006**, *417*, 273−279.

(14) Jang, H. S.; Yang, H.; Kim, S. W.; Han, J. Y.; Lee, S.-G.; Jeon, D. Y. White Light-Emitting Diodes with Excellent Color Rendering Based on Organically Capped CdSe Quantum Dots and $Sr_3SiO_5:Ce^{3+}$, Li^+ Phosphors. *Adv. Mater.* **2008**, *20*, 2696−2702.

(15) Mutlugun, E.; Hernandez-Martinez, P. L.; Eroglu, C.; Coskun, Y.; Erdem, T.; Sharma, V. K.; Unal, E.; Panda, S. K.; Hickey, S. G.; Gaponik, N.; et al. Large-Area (over 50 cm × 50 cm) Freestanding Films of Colloidal InP/ZnS Quantum Dots. *Nano Lett.* **2012**, *12*, 3986−3993.

DOI: 10.1021/acs.jpclett.5b02433
J. Phys. Chem. Lett. 2016, 7, 495−503

(16) Chuang, P.-H.; Lin, C. C.; Liu, R. S. Emission-Tunable $CuInS_2$/ZnS Quantum Dots: Structure, Optical Properties, and Application in White Light-Emitting Diodes with High Color Rendering Index. *ACS Appl. Mater. Interfaces* **2014**, *6*, 15379−15387.
(17) Pust, P.; Weiler, V.; Hecht, C.; Tücks, A.; Wochnik, A. S.; Henß, A.-K.; Wiechert, D.; Scheu, C.; Schmidt, P. J.; Schnick, W. Narrow-Band Red-Emitting $Sr[LiAl_3N_4]:Eu^{2+}$ as a Next-Generation LED-Phosphor Material. *Nat. Mater.* **2014**, *13*, 891−896.
(18) Stoll, H.; Hoppe, R. Ein Neues Oxoplumbat (IV): $CsNa_3[PbO_4]$. *Rev. Chim. Min.* **1987**, *24*, 96−115.
(19) Protesescu, L.; Yakunin, S.; Bodnarchuk, M. I.; Krieg, F.; Caputo, R.; Hendon, C. H.; Yang, R. X.; Walsh, A.; Kovalenko, M. V. Nanocrystals of Cesium Lead Halide Perovskites ($CsPbX_3$, X = Cl, Br, and I): Novel Optoelectronic Materials Showing Bright Emission with Wide Color Gamut. *Nano Lett.* **2015**, *15*, 3692−3696.
(20) Xu, Y. K.; Adachi, S. Properties of Mn^{4+}-Activated Hexafluorotitanate Phosphors. *J. Electrochem. Soc.* **2011**, *158*, J58−J65.
(21) Adachi, S.; Abe, H.; Kasa, R.; Arai, T. Synthesis and Properties of Hetero-Dialkaline Hexafluorosilicate Red Phosphor $KNaSiF_6:Mn^{4+}$. *J. Electrochem. Soc.* **2012**, *159*, J34−J37.
(22) Adachi, S.; Takahashi, T. Direct Synthesis of $K_2SiF_6:Mn^{4+}$ Red Phosphor from Crushed Quartz Schist by Wet Chemical Etching. *Electrochem. Solid-State Lett.* **2009**, *12*, J20−J23.
(23) Oh, J. H.; Kang, H. J.; Eo, Y. J.; Park, H. K.; Do, Y. R. Synthesis of Narrow-Band Red-Emitting $K_2SiF_6:Mn^{4+}$ Phosphors for a Deep Red Monochromatic LED and Ultrahigh Color Quality Warm-White LEDs. *J. Mater. Chem. C* **2015**, *3*, 607−615.
(24) Sijbom, H. F.; Joos, J. J.; Martin, L. I. D. J.; Eeckhout, K. V.; Poelman, D.; Smet, P. F. Luminescent Behavior of the $K_2SiF_6:Mn^{4+}$ Red Phosphor at High Fluxes and at the Microscopic Level. *ECS J. Solid State Sci. Technol.* **2016**, *5*, R3040−R3048.
(25) Xu, Y. K.; Adachi, S. Properties of $Na_2SiF_6:Mn^{4+}$ and $Na_2GeF_6:Mn^{4+}$ Red Phosphors Synthesized by Wet Chemical Etching. *J. Appl. Phys.* **2009**, *105*, 013525.
(26) Wang, Z. L.; Liu, Y.; Zhou, Y. Y.; Zhou, Q.; Tan, H. Y.; Zhang, Q. H.; Peng, J. H. Red-Emitting Phosphors $Na_2XF_6:Mn^{4+}$ (X = Si, Ge, Ti) with High Colour-Purity for Warm White-Light-Emitting Diodes. *RSC Adv.* **2015**, *5*, 58136−58140.
(27) Arai, Y.; Adachi, S. Optical Transitions and Internal Vibronic Frequencies of MnF_6^{2-} Ions in Cs_2SiF_6 and Cs_2GeF_6 Red Phosphors. *J. Electrochem. Soc.* **2011**, *158*, J179−J183.
(28) Adachi, S.; Takahashi, T. Photoluminescent Properties of $K_2GeF_6:Mn^{4+}$ Red Phosphor Synthesized from Aqueous HF/$KMnO_4$ Solution. *J. Appl. Phys.* **2009**, *106*, 013516.
(29) Kasa, R.; Adachi, S. Mn-Activated K_2ZrF_6 and Na_2ZrF_6 Phosphors: Sharp Red and Oscillatory Blue-Green Emissions. *J. Appl. Phys.* **2012**, *112*, 013506.
(30) Arai, Y.; Takahashi, T.; Adachi, S. Photoluminescent Properties of $K_2SnF_6{\cdot}H_2O:Mn^{4+}$ Red Phosphor. *Opt. Mater.* **2010**, *32*, 1095−1101.
(31) Arai, Y.; Adachi, S. Optical Properties of Mn^{4+}-activated Na_2SnF_6 and Cs_2SnF_6 Red Phosphors. *J. Lumin.* **2011**, *131*, 2652−2660.
(32) Zhu, H. M.; Lin, C. C.; Luo, W. Q.; Shu, S. T.; Liu, Z. G.; Liu, Y. S.; Kong, J. T.; Ma, E.; Cao, Y. G.; Liu, R. S.; et al. Highly Efficient Non-Rare-Earth Red Emitting Phosphor for Warm White Light-Emitting Diodes. *Nat. Commun.* **2014**, *5*, 4312.
(33) Zhou, Q.; Zhou, Y. Y.; Liu, Y.; Wang, Z. L.; Chen, G.; Peng, J. H.; Yan, J.; Wu, M. M. A New and Efficient Red Phosphor for Solid-State Lighting: $Cs_2TiF_6:Mn^{4+}$. *J. Mater. Chem. C* **2015**, *3*, 9615−9619.
(34) Sekiguchi, D.; Nara, J.; Adachi, S. Photoluminescence and Raman Scattering Spectroscopies of $BaSiF_6:Mn^{4+}$ Red Phosphor. *J. Appl. Phys.* **2013**, *113*, 183516.
(35) Jiang, X. Y.; Pan, Y. X.; Huang, S. M.; Chen, X.; Wang, J. G.; Liu, G. K. Hydrothermal Synthesis and Photoluminescence Properties of Red Phosphor $BaSiF_6:Mn^{4+}$ for LED Applications. *J. Mater. Chem. C* **2014**, *2*, 2301−2306.
(36) Hoshino, R.; Adachi, S. Optical Spectroscopy of $ZnSiF_6{\cdot}6H_2O:Mn^{4+}$ Red Phosphor. *J. Appl. Phys.* **2013**, *114*, 213502.
(37) Setlur, A. A. Phosphors for LED-Based Solid-State Lighting. *Electrochem. Soc. Interface* **2009**, *18*, 32−36.
(38) Zhou, H.; Chen, Q.; Li, G.; Luo, S.; Song, T.-B.; Duan, H.-S.; Hong, Z.; You, J.; Liu, Y.; Yang, Y. Interface Engineering of Highly Efficient Perovskite Solar Cells. *Science* **2014**, *345*, 542−546.
(39) Deschler, F.; Price, M.; Pathak, S.; Klintberg, L. E.; Jarausch, D.-D.; Higler, R.; Hüttner, S.; Leijtens, T.; Stranks, S. D.; Snaith, H. J.; et al. High Photoluminescence Efficiency and Optically Pumped Lasing in Solution-Processed Mixed Halide Perovskite Semiconductors. *J. Phys. Chem. Lett.* **2014**, *5*, 1421−1426.
(40) Nedelcu, G.; Protesescu, L.; Yakunin, S.; Bodnarchuk, M. I.; Grotevent, M. J.; Kovalenko, M. V. Fast Anion-Exchange in Highly Luminescent Nanocrystals of Cesium Lead Halide Perovskites ($CsPbX_3$, X = Cl, Br, I). *Nano Lett.* **2015**, *15*, 5635−5640.
(41) Shirasaki, Y.; Supran, G. J.; Bawendi, M. G.; Bulovic, V. Emergence of Colloidal Quantum-Dot Light-Emitting Technologies. *Nat. Photonics* **2012**, *7*, 13−23.
(42) Ye, S.; Xiao, F.; Pan, Y. X.; Ma, Y. Y.; Zhang, Q. Y. Phosphors in Phosphor-Converted White Light-Emitting Diodes: Recent Advances in Materials, Techniques and Properties. *Mater. Sci. Eng., R* **2010**, *71*, 1−34.
(43) Nguyen, H.-D.; Lin, C. C.; Liu, R. S. Waterproof Alkyl Phosphate Coated Fluoride Phosphors for Optoelectronic Materials. *Angew. Chem., Int. Ed.* **2015**, *54*, 10862−10866.
(44) Trots, D. M.; Myagkota, S. V. High-Temperature Structural Evolution of Caesium and Rubidium Triiodoplumbates. *J. Phys. Chem. Solids* **2008**, *69*, 2520−2526.
(45) Zhao, Y.; Riemersma, C.; Pietra, F.; Koole, R.; de Mello Donegá, C.; Meijerink, A. High-Temperature Luminescence Quenching of Colloidal Quantum Dots. *ACS Nano* **2012**, *6*, 9058−9067.
(46) Wu, S. L.; Liu, Y.; Chang, J.; Zhang, S. F. Ligand Dynamic Effect on Phase and Morphology Control of Hexagonal $NaYF_4$. *CrystEngComm* **2014**, *16*, 4472−4477.
(47) Peng, Z. A.; Peng, X. Nearly Monodisperse and Shape-Controlled CdSe Nanocrystals via Alternative Routes: Nucleation and Growth. *J. Am. Chem. Soc.* **2002**, *124*, 3343−3353.

DOI: 10.1021/acs.jpclett.5b02433
J. Phys. Chem. Lett. 2016, 7, 495−503